

# Conformer-specific Infrared spectroscopy of cationic Criegee intermediates *syn*- and *anti*-CH<sub>3</sub>CHOO<sup>+</sup>

Received: 11 August 2024

Accepted: 25 February 2025

Published online: 08 March 2025

Check for updates

Ende Huang<sup>1,2</sup>, Licheng Zhong<sup>1,3</sup>, Jingning Xue<sup>4</sup>, Xiaohu Zhou<sup>1</sup>, Siyue Liu<sup>1,5</sup>, Li Che<sup>4</sup>, Hongwei Li<sup>1,2</sup>, Hongjun Fan<sup>1,2</sup>✉, Wenrui Dong<sup>1,2,6</sup>✉ & Xueming Yang<sup>1,6,7</sup>✉

Criegee intermediates are pivotal in atmospheric chemistry, yet their cationic forms remain poorly understood. This study presents the infrared spectra of cationic Criegee intermediates, specifically *syn*- and *anti*-CH<sub>3</sub>CHOO<sup>+</sup>, using vacuum ultraviolet photoionization coupled with IR photon dissociation spectroscopy. Combined with quantum chemistry calculations, we explore conformer-specific infrared spectra and identify distinct unimolecular reaction pathways for each conformer. Our method reveals structural differences between neutral and cationic CH<sub>3</sub>CHOO, including a lower isomerization barrier in the cationic form. This approach enables the investigation of conformer-specific IR spectroscopy for cationic species, which is challenging using direct IR absorption methods. By exploiting these distinct reaction pathways, we can conduct conformer-specific spectroscopic studies, advancing our ability to trace specific molecular conformations in complex chemical processes in both atmospheric and interstellar contexts.

Criegee intermediates (CIs), carbonyl oxides generated during alkene ozonolysis<sup>1</sup>, are pivotal in atmospheric chemistry<sup>2</sup>. These highly reactive species influence the oxidative capacity of the atmosphere and contribute to hydroxyl radical<sup>3</sup> and aerosol<sup>4,5</sup> formation. The successful laboratory preparation of a substantial concentration of the simplest CIs (CH<sub>2</sub>OO)<sup>6</sup> has sparked extensive research into their reactivity<sup>7–10</sup>, spectroscopy<sup>7,11–13</sup>, and atmospheric implications<sup>2,14,15</sup>.

Among CIs, CH<sub>3</sub>CHOO has attracted significant attention due to its atmospheric prevalence<sup>2,16</sup> and its existence in two conformers: *syn*- and *anti*-CH<sub>3</sub>CHOO. These conformers differ in the orientation of the C–O–O group relative to the methyl group. Comprehensive studies have explored the neutral forms of these species, including their spectroscopic characteristics<sup>11,13,17,18</sup>, unimolecular and bimolecular reactions<sup>19–22</sup>, and photodissociation dynamics<sup>23,24</sup>.

IR spectroscopic investigations of neutral CH<sub>3</sub>CHOO have been conducted across various spectral regions. Fourier-transform infrared (FTIR) spectroscopy has been used to investigate the IR spectra of both *syn*- and *anti*-CH<sub>3</sub>CHOO conformers in the 830–1550 cm<sup>−1</sup> region<sup>25</sup>. Action spectroscopy methods have been extensively utilized to examine other spectral regions, including the CH stretch overtone<sup>11</sup>, combined bands ( $\nu_{CH} + \nu_i$ )<sup>21</sup>, and the CH stretch regions<sup>26</sup>, by detecting OH products through laser-induced fluorescence. The spectra obtained from the latter two regions have provided valuable insights into tunneling processes. However, the IR spectra of neutral *anti*-CH<sub>3</sub>CHOO in the mid-IR region remain elusive. This is due to two primary factors: the weak transition intensity of *anti*-CH<sub>3</sub>CHOO, which makes it unsuitable for FTIR analysis, and its high barriers for unimolecular reaction, rendering it

<sup>1</sup>State Key Laboratory of Molecular Reaction Dynamics, Dalian Institute of Chemical Physics, Chinese Academy of Sciences, Dalian, China. <sup>2</sup>University of Chinese Academy of Sciences, Beijing, China. <sup>3</sup>College of Chemical Engineering, Shenyang University of Chemical Technology, Shenyang, China.

<sup>4</sup>Department of Physics, School of Science, Dalian Maritime University, Dalian, Liaoning, China. <sup>5</sup>Key Laboratory of Materials Modification by Laser, Ion, and Electron Beams, Chinese Ministry of Education, School of Physics, Dalian University of Technology, Dalian, China. <sup>6</sup>Hefei National Laboratory, Hefei, China.

<sup>7</sup>Department of Chemistry, Southern University of Science and Technology, Shenzhen, China. ✉ e-mail: [fanhj@dicp.ac.cn](mailto:fanhj@dicp.ac.cn); [wrdong@dicp.ac.cn](mailto:wrdong@dicp.ac.cn); [xmyang@dicp.ac.cn](mailto:xmyang@dicp.ac.cn)

inappropriate for action spectroscopy methods that rely on observing dissociation products.

While IR spectra of neutral CIs have been extensively studied, knowledge about their cationic species remains scarce. This study presents the IR spectra of cationic CIs, specifically focusing on *syn*- and *anti*-CH<sub>3</sub>CHOO<sup>+</sup>. Our approach combines vacuum ultraviolet (VUV) photoionization for cationic radical preparation with IR photon dissociation spectroscopy. Quantum chemistry calculations were employed to optimize the experimental design, particularly in selecting appropriate VUV wavelengths to access specific unimolecular reaction channels for conformer-specific spectroscopic studies. These calculations also aided in assigning observed transitions to specific vibrational modes. This methodology enables the investigation of conformer-specific IR spectroscopy by exploiting the distinct unimolecular reaction pathways of the two conformers.

This study introduces a useful method for exploring the conformer-specific IR spectroscopy of cationic species, which is elusive from using the direct IR absorption method, by selecting the appropriate VUV wavelength for photoionization. This approach may have far-reaching implications, particularly in the field of interstellar chemistry, where intense mid-IR emission bands are frequently attributed to highly vibrationally excited polycyclic aromatic hydrocarbons (PAHs) in their cationic states<sup>27</sup>. The conformer selectivity afforded by our method has the potential to significantly enhance our ability to trace the origins of these species to specific molecular conformations, thereby advancing our understanding of complex interstellar chemical processes.

## Results

### VUV photoionization mass spectra of CH<sub>3</sub>CHOO

Figure 1a displays the time-of-flight (TOF) mass spectrum of CH<sub>3</sub>CHI<sub>2</sub>/O<sub>2</sub>/He mixture, obtained using 118 nm (10.5 eV) radiation. The spectrum revealed the parent ion signal of CH<sub>3</sub>CHI<sub>2</sub> at *m/z* = 282, along with fragment ions at *m/z* = 155 and 27, resulting from the photoionization dissociation of CH<sub>3</sub>CHI<sub>2</sub><sup>28</sup>.

Upon photolysis of the mixture with a 266 nm laser, additional mass spectral signals appeared at *m/z* = 15, 43, 44, 60, and 127 (Fig. 1b). The *m/z* = 60 signal corresponds to *syn*- and *anti*-CH<sub>3</sub>CHOO

conformers, while *m/z* = 44 signal is attributed to CH<sub>3</sub>CHO, a known photolysis product of both conformers<sup>23</sup>. Although the precise C-I bond dissociation energy of CH<sub>3</sub>CHI<sub>2</sub> remains undetermined, it is estimated to be -55 kcal mol<sup>-1</sup>, based on analogous molecules such as CH<sub>2</sub>I<sub>2</sub> and C<sub>2</sub>H<sub>5</sub>I<sup>29</sup>. Consequently, 266 nm photolysis could impart up to 52.5 kcal mol<sup>-1</sup> of internal energy to the CH<sub>3</sub>CHI radical. The subsequent reaction between CH<sub>3</sub>CHI and O<sub>2</sub>, forming CH<sub>3</sub>CHOO, has a calculated exothermicity of 46.5 kcal mol<sup>-1</sup><sup>30</sup>. This suggests that the internal energy of CH<sub>3</sub>CHOO could potentially reach 99 kcal mol<sup>-1</sup> under our experimental conditions. At such high internal energies, CH<sub>3</sub>CHOO may undergo dissociation to form acetaldehyde and O(D)<sup>23,31</sup>. The observed appearance energy of the *m/z* = 44 peaks (Supplementary Fig. S1) correlate well with the established ionization energy of the acetaldehyde (10.22 eV)<sup>32</sup>, supporting our analysis.

The mass spectral signal observed at *m/z* = 15 is attributed to CH<sub>3</sub> radical, which originates from the unimolecular decomposition of internally excited *syn*- and *anti*-CH<sub>3</sub>CHOO conformers. These conformers possess sufficient internal energy to surmount the transition state (TS9 in Fig. 2a) barrier of 31 kcal mol<sup>-1</sup>. While these excited conformers can theoretically generate vinyloxy radical (*m/z* = 43), this species remains undetectable in our mass spectra due to its high ionization energy (10.85 eV)<sup>33</sup>, which exceeds the energy of the 118 nm probe photon.

The observed signal at *m/z* = 43 is assigned to the dissociation products of *syn*- and *anti*-CH<sub>3</sub>CHOO<sup>+</sup> from 118 nm photoionization. As indicated in Fig. 2, assuming the ejected photoelectron carries negligible kinetic energy, the internal energy of the *syn*- and *anti*-CH<sub>3</sub>CHOO<sup>+</sup> is estimated to be 29 and 34 kcal mol<sup>-1</sup>, respectively. For the *syn*-CH<sub>3</sub>CHOO<sup>+</sup>, this energy content is sufficient to overcome both TS8 (18.5 kcal mol<sup>-1</sup>) and TS14 (20.4 kcal mol<sup>-1</sup>) barriers, leading to the formation of CH<sub>2</sub>CHO<sup>+</sup> (*m/z* = 43). The *anti*-CH<sub>3</sub>CHOO<sup>+</sup> can undergo isomerization to *syn*-CH<sub>3</sub>CHOO<sup>+</sup> either through a direct pathway via TS2 (26.5 kcal mol<sup>-1</sup>) or through a sequential pathway involving TS6 (13.9 kcal mol<sup>-1</sup>) followed by TS5 (17.5 kcal mol<sup>-1</sup>), subsequently generating CH<sub>2</sub>CHO<sup>+</sup>.

The mass spectra of the mixture exposed to the IR laser (2867 cm<sup>-1</sup>) following 266 and 118 nm laser irradiation are presented in Fig. 1c, with an enlarged view of *m/z* = 15, 43, 44, and 60 shown in

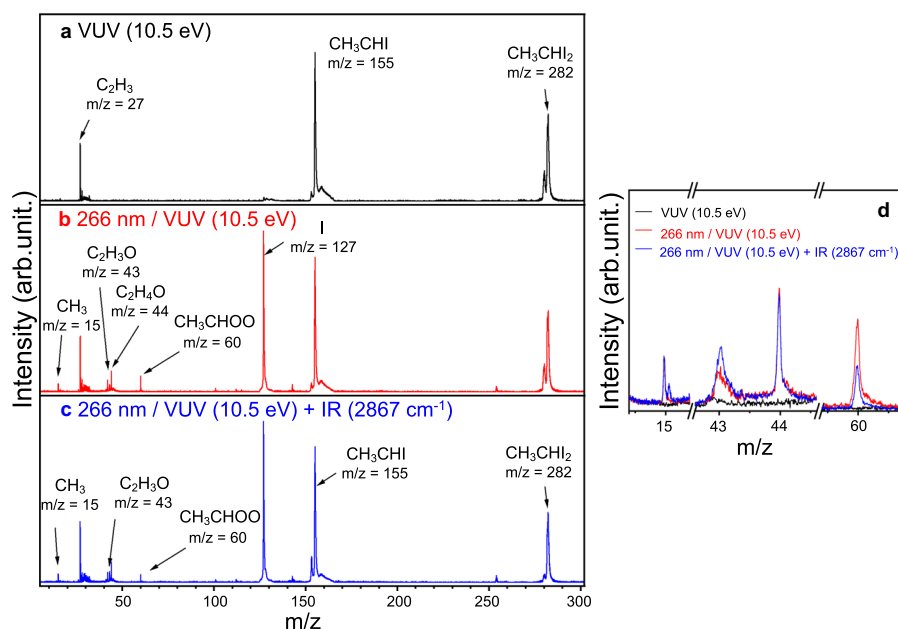


**Fig. 1 | TOF mass spectra of 1,1-diiodoethane seeded in a 20% O<sub>2</sub>/He mixture under various experimental conditions. a** Ionization with 118 nm VUV radiation. **b** 266 nm photolysis along a quartz capillary tube, followed by 118 nm VUV

photoionization. **c** 266 nm photolysis and 118 nm VUV photoionization, followed by IR laser absorption (2867 cm<sup>-1</sup>) 50 ns after VUV ionization. **d** Comparison of signal intensities at *m/z* = 15, 43, 44, and 60 under the conditions described in (a–c).

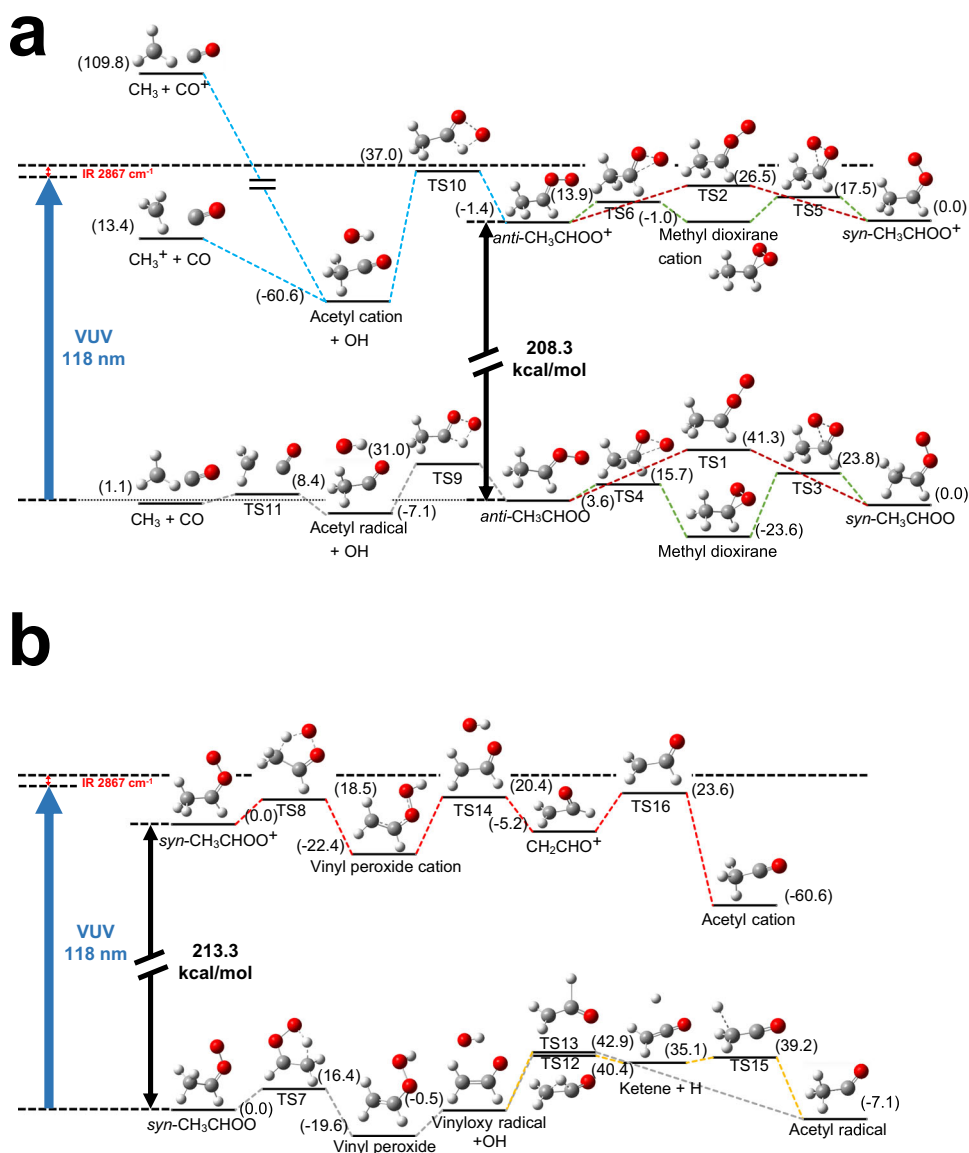


**Fig. 2 | Reaction coordinates for the isomerization and decomposition pathways of both neutral and cationic CH<sub>3</sub>CHOO.** **a** Pathways for isomerization and decomposition of neutral and cationic *anti*-CH<sub>3</sub>CHOO. **b** Pathway for decomposition of neutral and cationic *syn*-CH<sub>3</sub>CHOO. The energies of *syn*-CH<sub>3</sub>CHOO (lower panel) and *syn*-CH<sub>3</sub>CHOO<sup>+</sup> (top) are set to zero for comparative purposes.

Molecular geometries were optimized using the B2PLYP-D3 functional with the cc-pVTZ basis set. Energy calculations (in kcal mol<sup>-1</sup>) were performed at the DLPNO-CCSD(T)/aug-cc-pVTZ level of theory, based on the B2PLYP-D3/cc-pVTZ optimized geometries. All calculations were conducted using the ORCA program package and included zero-point energy corrections.

Fig. 1d. Notably, Fig. 1d reveals two distinct sources of CH<sub>3</sub><sup>+</sup> (*m/z* = 15). The first source arises from unimolecular reactions of internally excited *syn*- and *anti*-CH<sub>3</sub>CHOO, occurring independently of the IR laser. In contrast, the second source involves the IR-induced dissociation of cationic *syn*- and *anti*-CH<sub>3</sub>CHOO. This IR dissociation pathway is characterized by a peak at a mass-to-charge ratio slightly higher than 15, attributed to the delayed formation of CH<sub>3</sub><sup>+</sup>.

The observed delay in CH<sub>3</sub><sup>+</sup> formation can be explained by the initial existence of *syn*- and *anti*-CH<sub>3</sub>CHOO<sup>+</sup> until the arrival of the IR laser, 50 ns after the 118 nm laser pulse. The greater mass of *syn*- and *anti*-CH<sub>3</sub>CHOO<sup>+</sup> compared to CH<sub>3</sub><sup>+</sup> results in a reduced flight velocity, consequently delaying the arrival time of CH<sub>3</sub><sup>+</sup> generated via IR dissociation relative to those produced through direct 118 nm ionization.

Our experiments reveal that CH<sub>3</sub>CHO<sup>+</sup> (*m/z* = 44) signal is unresponsive to IR radiation. The dissociation of *syn*- and *anti*-CH<sub>3</sub>CHOO<sup>+</sup> to CH<sub>3</sub>CHO<sup>+</sup> and O(<sup>1</sup>D) or O(<sup>3</sup>P)) is expected to require excitation to an electronic excited state, similar to neutral *syn*- and *anti*-CH<sub>3</sub>CHOO.

This process necessitates -80 kcal mol<sup>-1</sup><sup>31</sup>, exceeding the energy available under the current experimental conditions, thus explaining the unresponsiveness of the CH<sub>3</sub>CHO<sup>+</sup> (*m/z* = 44) signal to IR radiation.

In contrast, when the IR laser is fired 50 ns after the 118 nm VUV laser, we observe an increase in CH<sub>3</sub><sup>+</sup> (*m/z* = 15) and C<sub>2</sub>H<sub>3</sub>O<sup>+</sup> (*m/z* = 43) signals, accompanied by a decrease in *m/z* = 60 signals. The origin of these cations is discussed in detail in the subsequent section.

### Unimolecular reaction pathways for neutral and cationic CH<sub>3</sub>CHOO

Figure 2 illustrates the reaction coordinates for the isomerization and decomposition of *syn*- and *anti*-CH<sub>3</sub>CHOO conformers and their corresponding cations. Supplementary Table S1 presents the single-point energies of optimized structures, including zero-point energy corrections. Under the experimental conditions employed, the initially formed *syn*- and *anti*-CH<sub>3</sub>CHOO species in the capillary tube possess internal energies up to 99 kcal mol<sup>-1</sup>. This energy is sufficient to

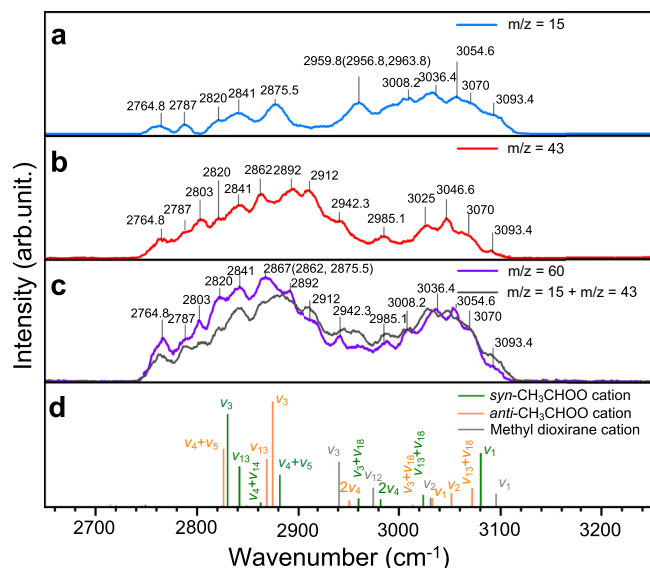


**Fig. 3 | Experimental and calculated IR spectra of *syn*- and *anti*-CH<sub>3</sub>CHOO<sup>+</sup>, as well as methyl dioxirane cation, in the 2700–3200 cm<sup>-1</sup> region.** Spectra were obtained by monitoring the ion signal at **a**  $m/z = 15$ , **b**  $m/z = 43$ , and **c**  $m/z = 60$ . For (**a**, **b**), the spectra were obtained by subtracting the ion signals recorded without IR radiation (266 nm and 118 nm only) from those recorded with IR radiation applied 50 ns after the 266 nm and 118 nm radiation. For the  $m/z = 60$  channel (**c**), to facilitate direct comparison, the subtraction was performed in reverse order (IR-off minus IR-on signals). Anharmonic IR stick spectra **d** were calculated using B2PLYP-D3/cc-pVTZ level of theory. Prominent transitions are indicated on the spectra.

facilitate isomerization between the *syn*- and *anti*-CH<sub>3</sub>CHOO conformers. Even though the formation of methyl dioxirane is feasible from the energy point of view, as shown in Fig. 2a, previous experiment exhibits no discernible of it from the photoionization efficiency spectroscopy<sup>7</sup>, indicating its formation is negligible. These energized species may subsequently decompose into various products, including vinyloxy, acetyl, methyl, and hydroxyl radicals, along with carbon monoxide. Alternatively, collisions within the capillary tube and during the ensuing supersonic expansion can thermalize these species, resulting in a typical rotational temperature of -10 K for *syn*- and *anti*-CH<sub>3</sub>CHOO<sup>11</sup>. Therefore, in the ionization region of the reflectron time-of-flight (TOF) mass spectrometer, all species possess negligible internal energy.

The ionization of cooled *syn*- and *anti*-CH<sub>3</sub>CHOO using a 118 nm laser imparts excess energy of 29 and 34 kcal mol<sup>-1</sup> to the initially formed *syn*- and *anti*-CH<sub>3</sub>CHOO cations, respectively. These energies exceed those of the transition states TS2, TS5, and TS6, enabling isomerization processes. Consequently, both *syn*- and *anti*-CH<sub>3</sub>CHOO<sup>+</sup> can interconvert and transform into methyl dioxirane cation. Our combined computational and experimental findings indicate minimal formation of vinyl peroxide cation through TS8 isomerization of *syn*-CH<sub>3</sub>CHOO<sup>+</sup>. This finding is corroborated by the absence of absorption in our experimental IR spectra (Supplementary Fig. S2) where B2PLYPD3/cc-pVTZ VPT2 calculations predict a strong O-H absorption band for the vinyl peroxide cation at 3501.7 cm<sup>-1</sup> (intensity 351.9 km mol<sup>-1</sup>).

*syn*-CH<sub>3</sub>CHOO<sup>+</sup> can undergo decomposition to OH and CH<sub>2</sub>CHO<sup>+</sup> through transition states TS8 and TS14. *anti*-CH<sub>3</sub>CHOO<sup>+</sup> exhibits two distinct isomerization pathways: it can either convert to methyl dioxirane cations via TS6 followed by isomerization to *syn*-CH<sub>3</sub>CHOO cation through TS5, or directly isomerize to *syn*-CH<sub>3</sub>CHOO<sup>+</sup> via TS2. Both pathways ultimately lead to decomposition processes analogous to those observed in directly formed *syn*-CH<sub>3</sub>CHOO cations.

We introduced an IR laser scanning from 2700 to 3200 cm<sup>-1</sup> region to the ionization region with a 50 ns delay following the 118 nm laser pulse. The resonance absorption of IR radiation by *syn*-/*anti*-CH<sub>3</sub>CHOO cations and methyl dioxirane cations may initiate additional unimolecular reaction channels. This absorption also enhances the probability of OH and CH<sub>2</sub>CHO<sup>+</sup> production due to the increased total energy of the system.

The ionization of neutral *anti*-CH<sub>3</sub>CHOO generates a diverse population of cationic species, predominantly *anti*-CH<sub>3</sub>CHOO<sup>+</sup>, but also including some *syn*-CH<sub>3</sub>CHOO<sup>+</sup> and methyl dioxirane cation resulting from isomerization. Upon absorption of an infrared photon near 3000 cm<sup>-1</sup>, these species achieve an energy level of -42.6 kcal mol<sup>-1</sup>, exceeding the TS10 barrier and facilitating the formation of acetyl cation and hydroxyl radical. Subsequently, the acetyl cation undergoes further decomposition to yield methyl cation and carbon monoxide. In contrast, cations derived from *syn*-CH<sub>3</sub>CHOO ionization reach only 37.6 kcal mol<sup>-1</sup> after similar IR absorption, barely surpassing the TS10 barrier. Under these energetic conditions, these species preferentially undergo decomposition through the lower-energy transition states TS8 and TS14 to form OH and CH<sub>2</sub>CHO<sup>+</sup>, rather than proceeding along the higher-energy pathway leading to methyl cation formation.

In summary, *anti*-CH<sub>3</sub>CHOO<sup>+</sup> exhibit two primary decomposition pathways upon absorption of IR radiation. The first involves the formation of acetyl cation ( $m/z = 43$ ) and methyl cation ( $m/z = 15$ ) via a high-energy transition state (TS10), while the second leads to CH<sub>2</sub>CHO<sup>+</sup> ( $m/z = 43$ ) through multiple lower-energy transition states (TS2 (or TS6 and TSS), TS8, and TS14). Methyl dioxirane cations that isomerize from *anti*-CH<sub>3</sub>CHOO<sup>+</sup> demonstrate similar reaction mechanisms upon absorption of IR radiation. In contrast, *syn*-CH<sub>3</sub>CHOO cations preferentially decompose into CH<sub>2</sub>CHO<sup>+</sup> and hydroxyl radicals via two low-energy transition states (TS8 and TS14) when exposed to IR radiation.

Based on these findings, we postulate that the observed production of  $m/z = 15$  species upon IR irradiation is predominantly attributed to *anti*-CH<sub>3</sub>CHOO<sup>+</sup>, with potential contributions from methyl dioxirane cation. The contribution from *syn*-CH<sub>3</sub>CHOO<sup>+</sup> to this product is likely negligible. Conversely, the formation of  $m/z = 43$  species is expected to originate from both *syn*- and *anti*-CH<sub>3</sub>CHOO<sup>+</sup>, with certain contributions from methyl dioxirane cation. We applied this hypothesis to assign the observed IR spectra in subsequent analyses, and our spectral observations further corroborated this assumption.

### Computed IR absorption spectra

Geometry optimizations and anharmonic vibrational frequency calculations for the *syn*- and *anti*-CH<sub>3</sub>CHOO<sup>+</sup> and methyl dioxirane cation were performed using the B2PLYP-D3 double-hybrid density functional theory approach with the cc-pVTZ basis set, based on its previously demonstrated reliability<sup>26,34,35</sup>. A comprehensive study of various computational methods for predicting the IR spectra of *anti*-CH<sub>3</sub>CHOO<sup>+</sup> revealed that B2PLYP-D3/cc-pVTZ provides superior performance among all evaluated methods, yielding a mean absolute error (MAE) of 11.8 cm<sup>-1</sup> (Supplementary Table S2). This approach yields high-quality geometries and frequencies comparable to CCSD(T) results, but with significantly reduced computational demands. All calculations, including the optimization of relevant transition states, were performed using the Gaussian 16 software package.

The anharmonic vibrational frequencies and associated IR intensities in the CH stretch fundamental region (2700–3200 cm<sup>-1</sup>) for cationic *syn*-/*anti*-CH<sub>3</sub>CHOO and methyl dioxirane cation are illustrated in Fig. 3d. Supplementary Tables S3–S8 provide detailed numerical data and mode descriptions. The *syn*-CH<sub>3</sub>CHOO<sup>+</sup> exhibits 17 IR transitions, comprising four fundamental bands, three overtones, and ten combination bands. In comparison, theoretical calculations

predict 18 IR transitions for the *anti*-CH<sub>3</sub>CHOO<sup>+</sup>, including an additional combination band. Notably, the carbonyl oxide CH stretch ( $\nu_2$ ) of *anti*-CH<sub>3</sub>CHOO<sup>+</sup> demonstrates a substantial IR intensity of 10.8 km mol<sup>-1</sup>, whereas the corresponding stretch in *syn*-CH<sub>3</sub>CHOO<sup>+</sup> shows a significantly lower intensity of 0.11 km mol<sup>-1</sup>. For the methyl dioxirane cation, theoretical predictions indicate only four transitions with intensity exceeding 0.5 km mol<sup>-1</sup>.

In our calculation of *syn*-/*anti*-CH<sub>3</sub>CHOO<sup>+</sup> and methyl dioxirane cation, the MAE is 17.5 cm<sup>-1</sup>. Some larger deviations observed for *syn*- and *anti*-CH<sub>3</sub>CHOO<sup>+</sup> can be attributed to their unique electronic structure, open-shell character, and inherent complexities in predicting overtones and combination bands.

### Experimental IR spectra and assignment

IR spectra of *syn*- and *anti*-CH<sub>3</sub>CHOO<sup>+</sup> were acquired by monitoring the parent ion ( $m/z = 60$ ) and two fragment ions ( $m/z = 15$  and 43) while scanning the IR laser (0.05 cm<sup>-1</sup> s<sup>-1</sup>) in the 2700–3200 cm<sup>-1</sup> region (Fig. 3). Notably, the rotational features in the IR spectra of CH<sub>3</sub>CHOO<sup>+</sup> are unresolved, despite the use of a narrow linewidth IR laser (0.15 cm<sup>-1</sup>). This observation is particularly noteworthy, considering that the transition modes of *syn*-CH<sub>3</sub>CHOO in this region have been previously resolved<sup>26</sup>. Moreover, the CH<sub>3</sub>CHOO<sup>+</sup> exhibits structural and rotational characteristics similar to its neutral counterpart (Supplementary Table S9).

Several factors contribute to these spectral distinctions. The rapid decomposition of parent ions would lead to significant lifetime broadening. If we assume a typical dissociation lifetime of ~200 fs. This would result in an energy uncertainty of ~13 cm<sup>-1</sup>. The 118 nm laser ionization process imparts significant internal energy (29 and 34 kcal mol<sup>-1</sup>) to *syn*- and *anti*-CH<sub>3</sub>CHOO<sup>+</sup>, markedly different from their neutral counterparts, which maintain a rotational temperature of ~10 K under jet-cooled conditions<sup>26</sup>. Furthermore, our recorded IR spectrum represents a composite of signals from both cationic *syn*- and *anti*-conformers, and methyl dioxirane cation, whereas previously reported neutral CH<sub>3</sub>CHOO spectra exclusively involved the *syn*-conformer.

This interpretation gains support from the observed enhanced resolution in IR spectra when monitoring CH<sub>3</sub><sup>+</sup> ( $m/z = 15$ ), compared to those observing the parent ion ( $m/z = 60$ ) and CH<sub>2</sub>CHO<sup>+</sup> ( $m/z = 43$ ), as illustrated in Fig. 3a–c. The spectrum of  $m/z = 15$  incorporates contributions from the *anti*-CH<sub>3</sub>CHOO<sup>+</sup> and methyl dioxirane cation, whereas the spectra of the  $m/z = 60$  and  $m/z = 43$  encompass these two species along with *syn*-CH<sub>3</sub>CHOO<sup>+</sup>.

The IR spectra obtained by monitoring changes in the  $m/z = 15$  signal upon IR radiation are presented in Fig. 3a. Spectral line positions were determined through multipeak fitting procedures employing Gaussian profiles, as elaborated in Supplementary Fig. S3 and Table S10. The spectrum reveals three prominent peaks in the range of 2820–2875.5 cm<sup>-1</sup>, which are attributed to the three strongest transitions of *anti*-CH<sub>3</sub>CHOO<sup>+</sup> as depicted in Fig. 3d:  $\nu_4 + \nu_5$ ,  $\nu_{13}$ , and  $\nu_3$ . Additional peaks observed at 2764.8 and 2787 cm<sup>-1</sup> are assigned to the  $2\nu_5$  and  $\nu_4 + \nu_6$  transitions of *anti*-CH<sub>3</sub>CHOO<sup>+</sup>, respectively. These peaks exhibit greater intensity than predicted by theoretical calculations, possibly due to uncertainties in calculated transition intensities and/or modes involving carbonyl oxide CH in-plane wag that facilitates four-membered ring formation. The predicted transition positions aligned closely with the observed peaks, typically within a few wavenumbers, with the exception of a 27 cm<sup>-1</sup> discrepancy for the peak at 2841 cm<sup>-1</sup>.

In the higher frequency region of 3045–3080 cm<sup>-1</sup>, a distinct peak and shoulder structure are observed, corresponding to the two strong transitions shown in Fig. 3d:  $\nu_2$  (3054.6 cm<sup>-1</sup>) and  $\nu_{13} + \nu_{18}$  (3070 cm<sup>-1</sup>). The peak at 3093.4 cm<sup>-1</sup> is attributed to the  $\nu_1$  mode of the methyl dioxirane cation. This assignment is supported by our theoretical calculations and the absence of significant *anti*-CH<sub>3</sub>CHOO<sup>+</sup> transitions in this spectral region. In the range of 2950–3045 cm<sup>-1</sup>, we observe a

cluster of three peaks that likely arise from overlapping contributions of both *anti*-CH<sub>3</sub>CHOO<sup>+</sup> and methyl dioxirane cation. This interpretation is based on the correlation between observed peak positions and calculated transition intensities for both species. Detailed peak assignments are provided in Table 1.

Our spectra (Fig. 3a) exhibit eleven distinct peaks, of which seven are assigned to pure transitions of *anti*-CH<sub>3</sub>CHOO<sup>+</sup>. Notably, these assignments include five of the most intense transitions predicted by our theoretical calculations (Fig. 3d). The remaining three theoretically predicted modes for *anti*-CH<sub>3</sub>CHOO<sup>+</sup> overlap with transitions of the methyl dioxirane cation, collectively accounting for three observed peaks. An additional peak at 3093.4 cm<sup>-1</sup> is attributed to a transition of the methyl dioxirane cation.

Among the fourteen assigned transitions (Supplementary Table S10), twelve are associated with CH<sub>3</sub> group modes, including both fundamental modes (e.g., the transition at 2875.5 cm<sup>-1</sup> originating from the methyl out-of-plane symmetric CH stretch) and combination/overtone modes (e.g., the transition at 3008.2 cm<sup>-1</sup> arising from the combination of methyl out-of-plane symmetric CH stretch and HCCO torsion). These observations suggest that the excitation of CH<sub>3</sub> group vibrational modes promotes the dissociation of parent cations (*anti*-CH<sub>3</sub>CHOO<sup>+</sup> and methyl dioxirane cation) to produce  $m/z = 15$  fragments.

The IR spectra obtained from the  $m/z = 43$  channel are presented in Fig. 3b. Notably, the counter of these spectra more closely resembles the calculated IR spectra of *syn*- and *anti*-CH<sub>3</sub>CHOO<sup>+</sup> shown in Fig. 3d, where the IR transitions in the 2800–2950 cm<sup>-1</sup> region are substantially stronger than those in the 2950–3100 cm<sup>-1</sup> region. This similarity likely arises from methyl dioxirane cation contributing more significantly to the  $m/z = 15$  channel than to the  $m/z = 43$  channel, as evidenced by a stronger peak at 3093.4 cm<sup>-1</sup> in Fig. 3a compared to Fig. 3b.

The spectra in Fig. 3b comprise contributions from IR transitions of *syn*- and *anti*-CH<sub>3</sub>CHOO<sup>+</sup>, with minor contributions from methyl dioxirane cation. Consequently, Fig. 3b exhibits more peaks than Fig. 3a, although some peaks in Fig. 3b lack obvious structure due to the presence of neighboring stronger peaks. Certain peaks observed in both figures are attributed to IR transitions of *anti*-CH<sub>3</sub>CHOO<sup>+</sup> and methyl dioxirane cation, as previously discussed.

Eight unassigned peaks in Fig. 3b originate from IR absorption of *syn*-CH<sub>3</sub>CHOO<sup>+</sup>. All eight IR transitions stronger than 1 km mol<sup>-1</sup>, labeled in Fig. 3d, have been assigned to the observed peaks based on calculated line positions and absorption intensities. The peak at 2803.0 cm<sup>-1</sup> is assigned to the  $2\nu_5$  vibrational mode, with a possible contribution from weak transition mode  $\nu_4 + \nu_6$ . Similarly, the peak at 2862.0 cm<sup>-1</sup> is primarily attributed to the  $\nu_3$  transition, potentially with a contribution from the weak transition mode  $\nu_4 + \nu_{14}$ . The comprehensive peak assignments are detailed in Table 1, with corresponding stick spectra provided in Supplementary Fig. S5.

The fragmentation of the parent ion  $m/z = 60$  (CH<sub>3</sub>CHOO<sup>+</sup> and methyl dioxirane cation) yields two principal fragments:  $m/z = 43$  (CH<sub>2</sub>CHO<sup>+</sup> and CH<sub>3</sub>CO<sup>+</sup>) and  $m/z = 15$  (CH<sub>3</sub><sup>+</sup>). The IR spectra obtained by monitoring these fragments (Fig. 3a, b) were combined and compared with the IR spectrum derived from the parent ion depletion in Fig. 3c. The combined spectral profile of the fragments closely matches that of the parent ion in the 2700–3200 cm<sup>-1</sup> region, with a notable exception of reduced intensity in the 2800–2870 cm<sup>-1</sup> range. A comprehensive comparison of IR spectra obtained by observing  $m/z = 15$ , 43, 44, and 60 is provided in Supplementary Fig. S4.

It is worth noting that discrepancies between action spectra profiles derived from parent ion observations and those from summed fragmentation products are not uncommon<sup>36,37</sup>. These differences can be attributed to various factors, including: (1) reduced signal-to-noise ratios in weak signals of fragment cations, and (2) mass-dependent detection efficiency of the MCP detector, where lighter cations typically exhibit higher detection efficiency than heavier ones. Specifically, the contribution from the  $m/z = 43$  fragment, which is more prominent

**Table 1 | Spectral peak assignments based on experimental observations, accompanied by calculated anharmonic frequencies, transition intensities, and transition types**

Position (cm <sup>-1</sup> )	Anharmonic frequency (cm <sup>-1</sup> )	<i>syn/anti</i> or dioxirane	Mode	IR intensity (km mol <sup>-1</sup> )	Transition type <sup>a</sup>		
					a	b	c
2764.8	2745.6	<i>anti</i> <sup>b</sup>	2V <sub>5</sub>	0.945	0.92	0.08	0.00
2787.0	2824.9	<i>anti</i>	V <sub>4</sub> + V <sub>6</sub>	0.746	0.35	0.65	0.00
2803.0	2749.2	<i>syn</i> <sup>c</sup>	2V <sub>5</sub>	1.35	0.96	0.04	0.00
2820.0	2826.1	<i>anti</i>	V <sub>4</sub> + V <sub>5</sub>	46.8	0.98	0.02	0.00
2841.0	2868.6	<i>anti</i>	V <sub>13</sub>	38.6	0.00	0.00	1.00
2862.0	2830.0	<i>syn</i>	V <sub>3</sub>	74.8	0.71	0.29	0.00
2875.5	2874.6	<i>anti</i>	V <sub>3</sub>	84.8	1.00	0.00	0.00
2892.0	2841.8	<i>syn</i>	V <sub>13</sub>	32.5	0.00	0.00	1.00
2912.0	2881.6	<i>syn</i>	V <sub>4</sub> + V <sub>5</sub>	25.7	0.92	0.08	0.00
2942.3	2960.4	<i>syn</i>	V <sub>3</sub> + V <sub>18</sub>	6.63	0.00	0.00	1.00
2956.8	2941.2	MDOX <sup>d</sup>	V <sub>3</sub>	36.3	0.96	0.04	0.00
2963.8	2951.1	<i>anti</i>	2V <sub>4</sub>	5.00	0.94	0.06	0.00
2985.1	2982.0	<i>syn</i>	2V <sub>4</sub>	5.99	0.02	0.98	0.00
2991.0	2974.7	MDOX	V <sub>12</sub>	15.2	0.00	0.00	1.00
3008.2	3013.3	<i>anti</i>	V <sub>3</sub> + V <sub>18</sub>	1.42	0.00	0.00	1.00
3022.6	3031.1	MDOX	V <sub>2</sub>	7.21	0.18	0.82	0.00
3025.0	3023.9	<i>syn</i>	V <sub>13</sub> + V <sub>18</sub>	9.69	0.89	0.11	0.00
3036.4	3033.0	<i>anti</i>	V <sub>1</sub>	6.82	0.03	0.97	0.00
3046.6	3080.5	<i>syn</i>	V <sub>1</sub>	43.1	0.39	0.61	0.00
3054.6	3051.5	<i>anti</i>	V <sub>2</sub>	10.8	0.76	0.24	0.00
3070.0	3072.0	<i>anti</i>	V <sub>13</sub> + V <sub>18</sub>	15.1	0.16	0.84	0.00
3093.4	3095.4	MDOX	V <sub>1</sub>	10.2	0.01	0.99	0.00

Tentative modes assignment was based on the calculated vibrational displacement vectors.

<sup>a</sup>The transition types (Type a, b, and c) are classified based on the direction of the transition dipole moment relative to the principal molecular axes (Supplementary Table S3–S5).

<sup>b</sup>"*anti*" denotes as *anti*-CH<sub>3</sub>CHOO<sup>+</sup>.

<sup>c</sup>"*syn*" denotes *syn*-CH<sub>3</sub>CHOO<sup>+</sup>.

<sup>d</sup>"MDOX" represents methyl dioxirane cation.

in the 2800–2870 cm<sup>-1</sup> range, may be underrepresented in the direct summation of fragment intensities due to its lower detection efficiency compared to *m/z* = 15 fragments.

The spectra of the *m/z* = 60 channel reveal a distinctive feature at 2867 cm<sup>-1</sup>, which is notably absent in the *m/z* = 15 and 43 channels. This feature arises from a combination of the *v*<sub>3</sub> transitions of both *syn*- and *anti*-CH<sub>3</sub>CHOO<sup>+</sup> conformers (2862 and 2875.5 cm<sup>-1</sup> in Fig. 3a, b). The observed peaks at 3025 and 3046.6 cm<sup>-1</sup> in Fig. 3b represent collective contributions from the dissociation of *syn*- and *anti*-CH<sub>3</sub>CHOO<sup>+</sup> and methyl dioxirane cation upon IR photon absorption, resulting in peak positions that differ from those of the individual species.

## Discussion

The *syn*- and *anti*-conformers of neutral CH<sub>3</sub>CHOO exhibit a substantial energy barrier of -41.3 kcal mol<sup>-1</sup> for direct interconversion (via TS1), primarily due to the rigid C=O double bond structure. This rigidity arises from the π bond, which requires substantial energy for bond rotation. However, an alternative, more energetically favorable pathway exists, which proceeds through TS3 and TS4, with methyl dioxirane as an intermediate. This pathway exhibits a notably lower transition state barrier of 23.8 kcal mol<sup>-1</sup> at TS3 compared to TS1.

In the case of cationic *syn*- and *anti*-CH<sub>3</sub>CHOO, both the direct conversion pathway (via TS2) and the methyl dioxirane-mediated route (via TS5, methyl dioxirane cation, and TS6) become more accessible due to significant electronic reorganization. Our computational analysis reveals that cationic *syn*- and *anti*-CH<sub>3</sub>CHOO structures exhibit enhanced charge delocalization compared to their neutral counterparts, resulting in a weakened C=O bond. This effect is quantitatively demonstrated by the Mayer bond order calculations,

showing a value of 1.331 for the transition state (TS2), lower than the 1.748 for the neutral transition state (TS1). The structural implication of this electronic reorganization is evident in the geometry of TS2, which features a C-O-O angle of 137.1° and an HCOO dihedral angle of 94.7° (Supplementary Fig. S6), indicating enhanced rotational freedom around the C-O bond.

These electronic and structural modifications significantly impact the energy of conformer interconversion in cationic species. The direct interconversion barrier between *syn*- and *anti*-CH<sub>3</sub>CHOO<sup>+</sup> is reduced to 26.5 kcal mol<sup>-1</sup>, while the methyl dioxirane-mediated pathway exhibits even lower barriers, with TS5 and TS6 requiring only 17.5 and 13.9 kcal mol<sup>-1</sup>, respectively.

Upon absorption of an IR photon, e.g., 2862 cm<sup>-1</sup>, the *syn*-CH<sub>3</sub>CHOO<sup>+</sup> possesses an internal energy of -37.2 kcal mol<sup>-1</sup>, which promotes a 1,4 H-transfer reaction, resulting in the formation of CH<sub>2</sub>CHO<sup>+</sup> and OH radical. Conformational changes of the aldehydic H in CH<sub>2</sub>CHO<sup>+</sup>, whether directed toward the methylene carbon or away from the aldehydic group, proceed through transition state TS16. Although the system possesses sufficient energy to overcome the TS16 barrier, the dissociation pathway may be kinetically hindered when the hydroxyl radical, generated from vinyl peroxide cation decomposition, retains significant internal energy. This mechanism provides a plausible explanation for the absence of characteristic *syn*-CH<sub>3</sub>CHOO<sup>+</sup> signatures in the IR spectra observed through the *m/z* = 15 channel.

The internal energy of *anti*-CH<sub>3</sub>CHOO<sup>+</sup> after absorption of an IR photon (2875 cm<sup>-1</sup>) is -42.2 kcal mol<sup>-1</sup>. Our computational analysis reveals that cationic *anti*-CH<sub>3</sub>CHOO follows a pathway comparable to its neutral counterpart, as depicted in Fig. 2a. In neutral *anti*-CH<sub>3</sub>CHOO, previous studies have demonstrated that the aldehydic

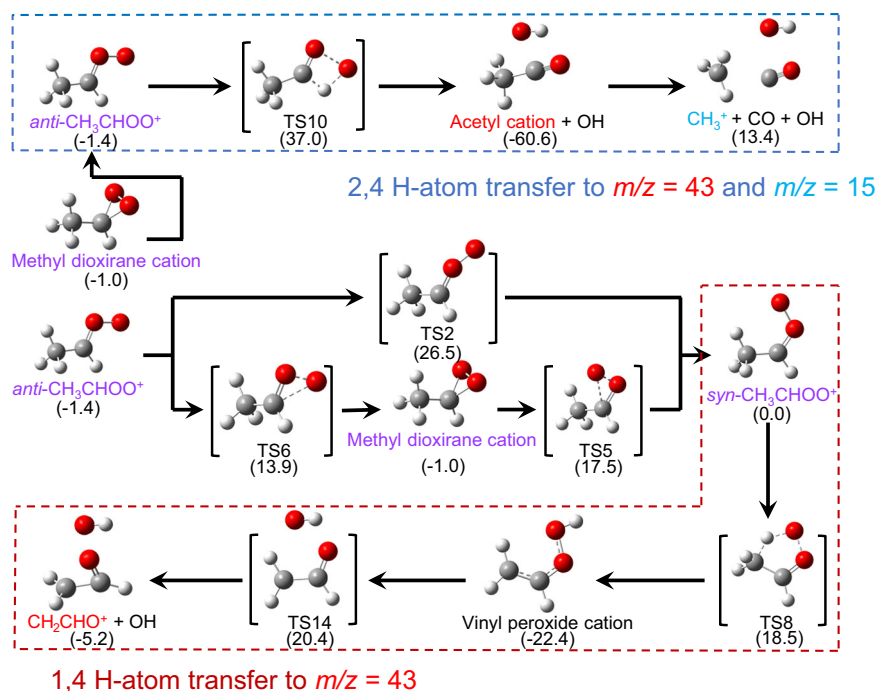


**Fig. 4 | Unimolecular decomposition pathways of *syn*-/*anti*-CH<sub>3</sub>CHOO<sup>+</sup> and methyl dioxirane cation, yielding fragment ions at *m/z* = 43 and *m/z* = 15. Energies (in kcal mol<sup>-1</sup>) are relative to *syn*-CH<sub>3</sub>CHOO<sup>+</sup>.**

hydrogen can transfer to the terminal peroxy oxygen, forming a four-membered ring structure<sup>38,39</sup> before dissociating into acetyl radical and hydroxyl radicals.

Quantum chemical calculations using Gaussian 16 reveal that the dissociation of cationic acetyl radicals (CH<sub>3</sub>CO<sup>+</sup>) into CH<sub>3</sub><sup>+</sup> and CO requires -74.0 kcal mol<sup>-1</sup> (Fig. 2a), consistent with the previously reported value of 70.5 kcal mol<sup>-1</sup><sup>40</sup>. The *anti*-CH<sub>3</sub>CHOO<sup>+</sup> possesses an internal energy of -42.2 kcal mol<sup>-1</sup>, which exceeds the energy barrier of transition state TS10. The subsequent decomposition yields CH<sub>3</sub>CO<sup>+</sup> and OH with a combined energy of 101.4 kcal mol<sup>-1</sup>. Under these energetic conditions, the acetyl cation likely retains sufficient internal energy to undergo further dissociation into CH<sub>3</sub><sup>+</sup> and CO. This process occurs without a reverse activation energy barrier, as even a slight elongation of the C-C bond in CH<sub>3</sub>CO<sup>+</sup> results in its direct dissociation into a methyl cation and neutral carbon monoxide, bypassing any intermediate transition state. This mechanism explains the observed dissociation of cationic *anti*-CH<sub>3</sub>CHOO to CH<sub>3</sub><sup>+</sup> upon IR absorption in our IR spectra of the *m/z* = 15 channel.

Although acetyl cations could theoretically dissociate to form methyl radicals, carbon monoxide cation, and hydroxyl radicals, this process requires energy exceeding 170.5 kcal mol<sup>-1</sup>. As this energy requirement falls outside the scope of our experimental conditions, we have not included this pathway in our analysis. Figure 4 illustrates the unimolecular decomposition pathways of *syn*-/*anti*-CH<sub>3</sub>CHOO and methyl dioxirane cations, yielding fragment ions at *m/z* = 43 and *m/z* = 15.

In summary, this study provides experimental and theoretical insights into the infrared spectroscopy of cationic CIs, specifically *syn*- and *anti*-CH<sub>3</sub>CHOO<sup>+</sup>. Our approach, combining VUV photoionization with IR photon dissociation spectroscopy, enables conformer-specific investigations that were previously challenging to achieve. Our quantum chemical calculations reveal structural differences between neutral and cationic CH<sub>3</sub>CHOO, highlighting a lower isomerization barrier in the cationic form due to enhanced charge delocalization. We have also extensively studied the unimolecular reaction pathways of these two conformers, providing a comprehensive understanding of their behavior.

This conformer-specific IR spectroscopic technique demonstrates broad potential for investigating various cationic species relevant to combustion, plasma chemistry, and astrochemistry. Beyond conformer identification, the method provides detailed structural information through IR spectral fingerprints and enables the elucidation of conformer-specific decomposition pathways through the combination of spectroscopic measurements with quantum chemistry calculations. Such capabilities are particularly valuable for understanding chemical evolution and energy transfer processes in these complex environments.

## Methods

### Experimental

The experimental setup comprised a molecular beam apparatus integrated with photolysis and probe lasers, a tunable IR laser, and a time-of-flight mass spectrometer (TOF-MS). The 1,1-diiodoethane precursor ( $\geq 98\%$ , Sigma-Aldrich) was soaked in glass paper and stored in a quartz cartridge container within an Even-Lavie valve. This precursor was entrained in a 20% O<sub>2</sub>/He carrier gas at a pressure of 16 atm. This gas mixture was expanded into a quartz capillary (1.5 mm inner diameter, 2.5 cm length) attached to the front flange of the valve, where the precursor was photolyzed by a 266 nm laser (20 mJ pulse<sup>-1</sup>, 10 Hz), the fourth harmonic of a Nd: YAG laser (Beamtech SGR-20, 10 Hz), to form the CH<sub>3</sub>CHI radical. The resulting CH<sub>3</sub>CHOO, produced from the reaction between CH<sub>3</sub>CHI and O<sub>2</sub>, was ionized by the 118 nm VUV laser (10 Hz).

A loosely focused tunable IR laser (5 Hz, bandwidth 0.15 cm<sup>-1</sup>) was fired 50 ns after the VUV laser, perpendicular to the molecular beam, exciting the cationic CH<sub>3</sub>CHOO at the center of the extraction region of the TOF mass spectrometer. This IR laser was generated using a potassium titanyl phosphate (KTP)/potassium titanyl arsenate (KTA) optical parametric oscillator/amplifier system (OPO/OPA, LaserVision) pumped by a Nd: YAG laser (Continuum Surelite EX). The typical pulse energy of the IR laser was 8–10 mJ.

IR spectra were obtained by scanning the IR laser from 2700 to 3200 cm<sup>-1</sup> at a rate of 0.05 cm<sup>-1</sup> s<sup>-1</sup>. The cationic CH<sub>3</sub>CHOO signal, with IR-on or IR-off, was amplified (SRS amplifier, SR445A) before being fed into an analog-to-digital converter card (Acqiris, SA220P, 2GS/s).

## Theoretical

All species involved in the unimolecular pathways were calculated using the B2PLYP-D3 functional with the cc-pVTZ basis set, as implemented in the Gaussian 16 program suite<sup>41</sup>. The vibrational second-order perturbation theory (VPT2) approach was employed to simulate equilibrium geometries, rotational constants, harmonic and anharmonic frequencies, and IR intensities for both *syn*- and *anti*-cationic CH<sub>3</sub>CHOO conformers.

Reaction coordinate energies were computed at the DLPNO-CCSD(T)/aug-cc-pVTZ//B2PLYP-D3/cc-pVTZ level of theory using the ORCA program, with zero-point energy corrections applied<sup>42</sup>. All energies are reported in kcal mol<sup>-1</sup>. Mayer bond orders were calculated using the Multifunctional Wavefunction Analyzer (Multiwfn) program<sup>43</sup>, based on wavefunctions obtained from Gaussian 16 calculations.

## Data availability

Data are provided with this paper and can be downloaded at <https://doi.org/10.6084/m9.figshare.28491056>. Source data are provided with this paper. Data supporting the findings of this manuscript are also available from the corresponding author upon request. Source data are provided with this paper.

## References

1. Criegee, R. Mechanism of ozonolysis. *Angew. Chem. Int. Ed.* **14**, 745–752 (1975).
2. Cox, R. A. et al. Evaluated kinetic and photochemical data for atmospheric chemistry: Volume VII—Criegee intermediates. *Atmos. Chem. Phys.* **20**, 13497–13519 (2020).
3. Emmerson, K. M. et al. Free radical modelling studies during the UK TORCH Campaign in Summer 2003. *Atmos. Chem. Phys.* **7**, 167–181 (2007).
4. Caravan, R. et al. Observational evidence for Criegee intermediate oligomerization reactions relevant to aerosol formation in the troposphere. *Nat. Geosci.* **17**, 219–226 (2024).
5. Chhantyal-Pun, R. et al. Criegee intermediate reactions with carboxylic acids: a potential source of secondary organic aerosol in the atmosphere. *ACS Earth Space Chem.* **2**, 833–842 (2018).
6. Welz, O. et al. Direct kinetic measurements of Criegee intermediate (CH<sub>2</sub>OO) formed by reaction of CH<sub>2</sub> with O<sub>2</sub>. *Science* **335**, 204–207 (2012).
7. Taatjes, C. A. et al. Direct measurements of conformer-dependent reactivity of the Criegee intermediate CH<sub>3</sub>CHOO. *Science* **340**, 177–180 (2013).
8. Su, Y. T. et al. Extremely rapid self-reaction of the simplest Criegee intermediate CH<sub>2</sub>OO and its implications in atmospheric chemistry. *Nat. Chem.* **6**, 477–483 (2014).
9. Chao, W., Hsieh, J. T., Chang, C. H. & Lin, J. J. Atmospheric chemistry. Direct kinetic measurement of the reaction of the simplest Criegee intermediate with water vapor. *Science* **347**, 751–754 (2015).
10. Chhantyal-Pun, R. et al. Criegee intermediates: production, detection and reactivity. *Int. Rev. Phys. Chem.* **39**, 383–422 (2020).
11. Liu, F., Beames, J. M., Petit, A. S., McCoy, A. B. & Lester, M. I. Infrared-driven unimolecular reaction of CH<sub>3</sub>CHOO Criegee intermediates to OH radical products. *Science* **345**, 1596–1598 (2014).
12. Beames, J. M., Liu, F., Lu, L. & Lester, M. I. Ultraviolet spectrum and photochemistry of the simplest Criegee intermediate CH<sub>2</sub>OO. *J. Am. Chem. Soc.* **134**, 20045–20048 (2012).
13. Sheps, L., Scully, A. M. & Au, K. UV absorption probing of the conformer-dependent reactivity of a Criegee intermediate CH<sub>3</sub>CHOO. *Phys. Chem. Chem. Phys.* **16**, 26701–26706 (2014).
14. Khan, M., Percival, C., Caravan, R., Taatjes, C. & Shallcross, D. Criegee intermediates and their impacts on the troposphere. *Environ. Sci. Proc. Impacts* **20**, 437–453 (2018).
15. Shallcross, D. E., Khan, M. A. H., Taatjes, C. A. & Percival, C. J. *New Insights into the Role of Stabilized Criegee Intermediates in Tropospheric Chemistry from Direct Laboratory Studies* (World Scientific, 2019).
16. Shabin, M., Kumar, A., Hakkim, H., Rudich, Y. & Sinha, V. Sources, sinks, and chemistry of stabilized Criegee intermediates in the Indo-Gangetic Plain. *Sci. Total Environ.* **896**, 165281 (2023).
17. Smith, M. C. et al. UV absorption spectrum of the C2 Criegee intermediate CH<sub>3</sub>CHOO. *J. Chem. Phys.* **141**, 074302 (2014).
18. Nakajima, M. & Endo, Y. Communication: spectroscopic characterization of an alkyl substituted Criegee intermediate *syn*-CH(3)CHOO through pure rotational transitions. *J. Chem. Phys.* **140**, 011101 (2014).
19. Zhou, X., Liu, Y., Dong, W. & Yang, X. Unimolecular reaction rate measurement of *syn*-CH<sub>3</sub>CHOO. *J. Phys. Chem. Lett.* **10**, 4817–4821 (2019).
20. Li, Y.-L., Kuo, M.-T. & Lin, J. J.-M. Unimolecular decomposition rates of a methyl-substituted Criegee intermediate *syn*-CH<sub>3</sub>CHOO. *RSC Adv.* **10**, 8518–8524 (2020).
21. Fang, Y. et al. Deep tunneling in the unimolecular decay of CH<sub>3</sub>CHOO Criegee intermediates to OH radical products. *J. Chem. Phys.* **145**, 234308 (2016).
22. Fang, Y. et al. Communication: Real time observation of unimolecular decay of Criegee intermediates to OH radical products. *J. Chem. Phys.* **144**, 061102 (2016).
23. Li, H., Fang, Y., Kidwell, N. M., Beames, J. M. & Lester, M. I. UV photodissociation dynamics of the CH<sub>3</sub>CHOO Criegee intermediate: action spectroscopy and velocity map imaging of O-atom products. *J. Phys. Chem. A* **119**, 8328–8337 (2015).
24. Kidwell, N. M., Li, H. W., Wang, X. H., Bowman, J. M. & Lester, M. I. Unimolecular dissociation dynamics of vibrationally activated CH<sub>3</sub>CHOO Criegee intermediates to OH radical products. *Nat. Chem.* **8**, 509–514 (2016).
25. Lin, H. Y. et al. Infrared identification of the Criegee intermediates *syn*- and *anti*-CH(3)CHOO, and their distinct conformation-dependent reactivity. *Nat. Commun.* **6**, 7012 (2015).
26. Barber, V. P., Pandit, S., Esposito, V. J., McCoy, A. B. & Lester, M. I. CH stretch activation of CH<sub>3</sub>CHOO: deep tunneling to hydroxyl radical products. *J. Phys. Chem. A* **123**, 2559–2569 (2019).
27. Oomens, J., Tielens, A., Sartakov, B. G., Von Helden, G. & Meijer, G. Laboratory infrared spectroscopy of cationic polycyclic aromatic hydrocarbon molecules. *Astrophys. J.* **591**, 968 (2003).
28. Siebert, M. R., Aquino, A. J. A., de Jong, W. A., Granucci, G. & Hase, W. L. Potential energy surface for dissociation including spin-orbit effects. *Mol. Phys.* **110**, 2599–2609 (2012).
29. Luo Y.-R. *Comprehensive Handbook of Chemical Bond Energies* (CRC Press, 2007).
30. Enami, S. et al. Formation of the iodine monoxide radical from gas-phase reactions of iodoalkyl radicals with molecular oxygen. *Chem. Phys. Lett.* **445**, 152–156 (2007).
31. Beames, J. M., Liu, F., Lu, L. & Lester, M. I. UV spectroscopic characterization of an alkyl substituted Criegee intermediate CH<sub>3</sub>CHOO. *J. Chem. Phys.* **138**, 244307 (2013).
32. Traeger, J. C. Heat of formation for the formyl cation by photoionization mass spectrometry. *Int. J. Mass Spectrom. Ion. Process.* **66**, 271–282 (1985).
33. Lambert, R., Christie, M. I., Golethorpe, R. & Linnett, J. W. Mass spectrometric study of the reaction of nitrogen atoms with acetaldehyde. *Proc. R. Soc. Lond. Ser. A Math. Phys. Sci.* **302**, 167–183 (1968).
34. Vazart, F., Latouche, C., Cimino, P. & Barone, V. Accurate Infrared (IR) Spectra for Molecules Containing the C · N Moiety by Anharmonic Computations with the Double Hybrid B2PLYP Density Functional. *J. Chem. Theory Comput.* **11**, 4364–4369 (2015).

35. Mitra, H. & Roy, T. K. Comprehensive benchmark results for the accuracy of basis sets for anharmonic molecular vibrations. *J. Phys. Chem. A* **124**, 9203–9221 (2020).
36. Hu, Y., Fu, H. & Bernstein, E. Infrared plus vacuum ultraviolet spectroscopy of neutral and ionic ethanol monomers and clusters. *J. Chem. Phys.* **125**, 154305 (2006).
37. Dopfer, O. et al. Protonation sites of isolated fluorobenzene revealed by IR spectroscopy in the fingerprint range. *J. Phys. Chem. A* **109**, 7881–7887 (2005).
38. Yin, C. & Takahashi, K. How does substitution affect the unimolecular reaction rates of Criegee intermediates? *Phys. Chem. Chem. Phys.* **19**, 12075–12084 (2017).
39. Dyakov, Y. A. et al. Isomerization and decay of a Criegee intermediate CH<sub>3</sub>CHO in the Earth's upper atmosphere. *Russ. J. Phys. Chem. B* **15**, 559–565 (2021).
40. Nobes, R. H., Bouma, W. J. & Radom, L. Structures and stabilities of gas-phase C<sub>2</sub>H<sub>3</sub>O<sup>+</sup> ions: an ab initio molecular orbital study. *J. Am. Chem. Soc.* **105**, 309–314 (1983).
41. Frisch, M. J. et al. Fox. Gaussian 16. Revision A03. (Gaussian Inc, 2016).
42. Neese, F. The ORCA program system. *Wiley Interdiscip. Rev. Comput. Mol. Sci.* **2**, 73–78 (2012).
43. Lu, T. & Chen, F. Multiwfn: a multifunctional wavefunction analyzer. *J. Comput. Chem.* **33**, 580–592 (2012).

## Acknowledgements

This work was funded by the National Natural Science Foundation of China (NSFC No. 22288201 (W.D.), 22473107 and 92461307 (H.F.)), the Scientific Instrument Developing Project of the Chinese Academy of Sciences (GJJSTD20220001 (X.Y.)), and the Innovation Program for Quantum Science and Technology (No. 2021ZD0303305 (W.D.)), the Guangdong Science and Technology Program (grants 2019ZT08L455 and 2019JC01X091 (X.Y.)) and the Shenzhen Science and Technology Program (grant ZDSYS2020042111001787 (X.Y.)). We thank the staff members of the Free Radical Detection Station (31127.02.DCLS.FRDS) at the Dalian Coherent Light Source (31127.02.DCLS) for providing technical support during the experiment.

## Author contributions

W.D., X.Y., and H.F. conceived and supervised the research. The experiments were carried out by E.H., L.Z., J.X., X.Z., S.L., L.C., H.L., and W.D. Data analysis and interpretation were performed by E.H., H.F., W.D., and X.Y. Theoretical calculations were performed by E.H. and H.F. The

manuscript was written by E.H., W.D., X.Y., and H.F., with contributions from all authors. All authors contributed to discussions about the content of the paper.

## Competing interests

The authors declare no competing interests.

## Additional information

**Supplementary information** The online version contains supplementary material available at <https://doi.org/10.1038/s41467-025-57670-4>.

**Correspondence** and requests for materials should be addressed to Hongjun Fan, Wenrui Dong or Xueming Yang.

**Peer review information** *Nature Communications* thanks Liming Wang, and the other anonymous reviewers for their contribution to the peer review of this work. A peer review file is available.

**Reprints and permissions information** is available at <http://www.nature.com/reprints>

**Publisher's note** Springer Nature remains neutral with regard to jurisdictional claims in published maps and institutional affiliations.

**Open Access** This article is licensed under a Creative Commons Attribution-NonCommercial-NoDerivatives 4.0 International License, which permits any non-commercial use, sharing, distribution and reproduction in any medium or format, as long as you give appropriate credit to the original author(s) and the source, provide a link to the Creative Commons licence, and indicate if you modified the licensed material. You do not have permission under this licence to share adapted material derived from this article or parts of it. The images or other third party material in this article are included in the article's Creative Commons licence, unless indicated otherwise in a credit line to the material. If material is not included in the article's Creative Commons licence and your intended use is not permitted by statutory regulation or exceeds the permitted use, you will need to obtain permission directly from the copyright holder. To view a copy of this licence, visit <http://creativecommons.org/licenses/by-nc-nd/4.0/>.

© The Author(s) 2025